Food Chemistry 476 (2025) 143482

Contents lists available at ScienceDirect

Food Chemistry

journal homepage: www.elsevier.com/locate/foodchem

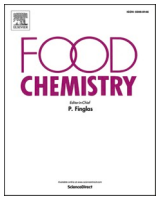

Fluorophore-labeled molecule recognition peptide: Static quenching in metal-organic frameworks for ultrasensitive ratiometric fluorescence biosensing of ochratoxin a in grain products

Li-Hong Yu, Yue-Hong Pang, Xiao-Fang Shen *

School of Food Science and Technology, Jiangnan University, Wuxi 214122, PR China

ARTICLE INFO

Keywords:
Molecular recognition peptide
Metal-organic frameworks
Static quenching
Ratiometric fluorescence biosensing
Ochratoxin a

ABSTRACT

Ochratoxin A (OTA) is a notable mycotoxin prevalent in grain products. In this paper, we computationally designed a high-affinity molecular recognition peptide (MRP, KQRLKCASLQKFGERAF) targeted at OTA according to structural analysis and molecular dynamics with a dissociation constant (K_d) of 12.18 ± 6.59 nM. A novel fluorescent probe, RhB-MRP (MRP-lysine-rhodamine B), was synthesized to convert the binding of MRP and OTA into optical signals. Based on RhB-MRP, we constructed a ratiometric fluorescence biosensor utilizing the classic blue fluorescent MOFs (NH_2-MIL-88(Fe)). The fluorescence of NH_2-MIL-88(Fe) was strongly quenched by RhB-MRP, which formed a ground state complex leading to static quenching. The developed biosensor exhibited exceptional sensitivity with detection limit of 0.32 pg mL^{-1} and rapid response time (11 min). A good recovery rate of 87.3–114.1 % was achieved in grain products. Although there are currently few MRPs that can specifically recognize small molecules, this highly sensitive and selective biosensor demonstrates the great potential of MRPs for detecting other molecules.

1. Introduction

Ochratoxin A (OTA), a hazardous secondary metabolite from Aspergillus and Penicillium fungi under natural conditions, seriously contaminates agro-products and fermented foods, such as corn, wheat, wine, and vinegar (Pandey, Samota, Kumar, Silva, & Dubey, 2023). The phenylalanyl derivative structure of substituted isocoumarin in OTA renders it highly toxic even at low concentrations (Song et al., 2022). It can inhibit protein synthesis, perturb metabolic pathways, and damage DNA in humans and animals (Tao et al., 2018). To reduce the risk of OTA exposure, most countries have set strict regulatory limits of OTA, such as the European Union, which has set a limit of 2 μg kg^{-1} for wine and 5 μg kg^{-1} for cereal (Ahn, Lee, Lee, & Kim, 2016; Su et al., 2022). The advancement in precise and rapid detection methods is essential for effective oversight in food safety. In recent years, fluorescence assay is attractive option for OTA detection due to their advantages of low cost, easy accessibility, and high sensitivity (Gao et al., 2019; Su et al., 2022). In particular, ratiometric fluorescence sensors possess significant potential for practical applications, as they are capable of correction deviations stemming from environmental factors and diverse equipment, thereby enhancing the overall stability and reliability of the sensors.

Nanomaterials have significantly advanced the creation and growth of ratiometric fluorescence probes in novel ways, such as ratiometric dual lanthanide nanoprobes (Qu, Wang, & You, 2020) and double fluorescence quantum dots (Xu et al., 2019). Among various optically active nanocrystals, metal-organic frameworks (MOFs) stand out due to their flexible porosity and size-tunable optical properties, positioning them as prime absorbers and fluorophores in fluorescence sensors (Metzger, Brozek, Comito, & Dinca, 2016). The self-fluorescence property of MOFs has been leveraged to develop a ratio fluorescent biosensor for the detection of exosome-derived miRNA (Sun et al., 2022). Our research group has capitalized on the porosity of MOFs by embedding rhodamine B (RhB) within them, thereby crafting a ratiometric fluorescence sensor for the detection of glyphosate (Wan, Pang, Feng, & Shen, 2022). Furthermore, the molar extinction coefficients of MOFs,

Abbreviations: OTA, Ochratoxin A; RhB, Rhodamine B; MRP, Molecule recognition peptide; RhB- MRP, MRP-lysine-rhodamine B; NHS, N-hydroxysuccinimide; EDC, 1-(3-Dimethylaminopropyl)-3-ethylcarbodiimide; BSA, Bovine serum albumin; MD, Molecular dynamics; SA-HRP, Streptavidin-horse radish peroxidase; K_d, Dissociation constant; RMSD, Root mean square deviations; IFE, Inner filter effect; LOD, Limit of detection; RSD, Relative standard deviation.

* Corresponding author.
E-mail address: xfshen@jiangnan.edu.cn (X.-F. Shen).

https://doi.org/10.1016/j.foodchem.2025.143482
Received 5 November 2024; Received in revised form 16 February 2025; Accepted 16 February 2025
Available online 18 February 2025

which are on the order of 10^8 cm^{-1} M^{-1} or higher, surpass those of conventional chromophores by several orders of magnitude (Zhang, Zhou, Tang, Hou, & Wu, 2019), marking MOFs as promising materials for fabricating ratio fluorescence sensors.

The selection of fluorescent sensors for OTA analysis primarily relies on the interaction with a specific recognition element to achieve detection, including antibodies and aptamers (Song et al., 2021; Wang et al., 2023; Wu et al., 2024). To date, the preference has largely been for aptamers due to their advantages over antibodies in terms of ease of preparation, high stability, and low cost (Chen et al., 2022; Xu et al., 2022). Since Cruz-Aguado and Penner identified an aptamer sequence (OBA36: 5′-GATCGGGTGTGGGTGGCGTAAAGGGAGCATCGGACA-3′) for OTA (Cruz-Aguado & Penner, 2008), various aptasensors have been developed for its rapid detection (Guo et al., 2021; Guo et al., 2022; Ren et al., 2022; H. Wang et al., 2022). A review of multiple fluorescent aptasensors for OTA reveals that the detection limits of these sensors are typically at the microgram-per-liter level, due to the binding affinity of OBA36 with OTA being approximately 0.2 μM (K_d). Therefore, there is a need to develop a recognition element with superior affinity that is also easy to prepare and highly stable for use in fluorescence or other rapid detection methods.

Molecule recognition peptide (MRP), which shares the fundamental structural unit with antibodies/proteins, exhibits potential as high-affinity bioreceptors. Computational design and screening have greatly increased the efficiency of obtaining high affinity peptides and have been widely used in drug design and bioscience (Dawson et al., 2023). Recently, our group introduced a method for computational design of MRPs based on molecular dynamics simulations (Yu et al., 2025). The accessibility, ease of labeling, strong analyte binding, biocompatibility, and high water-solubility of peptides have made them a popular choice in sensing (Huang et al., 2023). Recently, MRPs have been developed to recognize diverse targets, including virus (Mascini et al., 2021; Xu, Aikeremu, Wang, Li, & Li, 2023), disease marker (Guo, Wang, & Zhuang, 2019; Zhu & Zhou, 2022), pesticide (Wang et al., 2020), odor molecules (Homma et al., 2023), and metal ions (Neupane, Oh, Park, & Lee, 2016). These studies indicate that MRP has become a candidate for sensitive and specific sensing as bioreceptor.

The computationally designed MRPs address the time-consuming experimental screening and labor-intensive challenges associated with selecting recognition elements, such as molecular imprinting, aptamers, and antibodies. Furthermore, the phenolic and carboxyl groups in OTA impart strong polarity and hydrogen bonding properties, while the benzene ring and quinone group provide binding sites for peptide design, enabling the development of high-affinity MRPs. As a result, the MRPs show great potential for the development of sensitive and specific detection methods for OTA, utilizing their high affinity. And now, the peptide-based methods typically utilize field-effect transistors and electrochemical sensing to convert the binding signals of peptide to small molecules into electrical signals (Homma et al., 2023). Thus, how to design simpler signal transduction methods, so that the combination of highly specific MRP and small molecules can be converted into more easily measured optical signals, is an urgent problem to be solved in practical applications.

In this study, we designed a novel RhB-MRP probe and developed a RhB-MRP mediated ratiometric fluorescence biosensor utilizing NH_2-MIL-88(Fe), a classical fluorescent material of MOFs, for trace OTA detection. The MRP was firstly computational designed according to the structural analysis and molecular dynamic simulations. With the incorporation of NH_2-MIL-88(Fe), RhB-MRP could effectively transduces the binding of MPR and OTA into a measurable fluorescence signal, and also can be used as a built-in reference. The high affinity between MRP and OTA improves the sensitivity and specificity of the biosensor. The sensitive and rapid optical biosensor was developed based on RhB-MRP with the ability to identify OTA in grain and grain products.

2. Experimental section

2.1. Chemicals and reagents

The peptides, RhB label-peptide and biotin-peptide, both exceeding 95 % purity, were sourced from ChinaPeptides (Shanghai, China). All of the other reagents utilized were of the analytical grade. OTA and other mycotoxin standards were obtained from Pribolab (Qingdao, China). $FeCl_3$, concentrated sulfuric acid, NH_2-BDC, carbinol, and other chemicals were supplied by Sinopharm Chemical Reagent Co., Ltd. (Shanghai, China). N-hydroxysuccinimide (NHS), 1-(3-Dimethylaminopropyl)-3-ethylcarbodiimide (EDC) and bovine serum albumin (BSA) were procured from Aladdin Biochemical Technology Co., Ltd. (Shanghai, China).

2.2. Apparatus

Fluorescence spectrophotometer (F-7000, Hitachi, Japan) was used to collect fluorescence spectra data. For the measurements, the excitation and emission slit widths were set at 5 nm, with a voltage of 700 V, and an excitation wavelength of 365 nm. The absorbance intensity measurements were conducted with a Cytation 3 multimode microplate reader (BioTek, VT). To investigate the materials' morphological features, structural compositions, chemical functionalities, and elemental makeup, we employed a diverse set of analytical tools. These included the SU8100 scanning electron microscope (SEM) sourced from Hitachi in Japan for morphological examination, the IS10 FT-IR spectrometer from Nicolet in the USA for chemical group identification, the D2 PHASER X-ray diffractometer (XRD) manufactured by Bruker AXS in Germany for structural analysis, and finally, the Scientific KAlpha X-ray photoelectron spectroscopy (XPS) instrument from Thermo in the USA for elemental characterization.

2.3. The in-silico simulation of peptide and mycotoxins

Molecular dynamics (MD) simulations were performed for the peptide with mycotoxins using the GROMACS (version 2022.3; http://www.gromacs.org/), taking advantage of CUDA acceleration. The ligand molecules were constructed using the DFT/B3LYP method with a 6-311G** basis set in Gaussian 09 (C. 01), and the RESP charges were fitted using the Antechamber tool.

For all MD simulations, we employed the AMBER99SB-ILDN force field along with TIP3P explicit water (Palazzesi, Prakash, Bonomi, & Barducci, 2015). The complex structure was centered in a cubic box, maintaining a minimum distance of 1 nm from the box edges. The remaining space in the box was filled with TIP3P water molecules, and the systems were neutralized by adding appropriate numbers of chlorine and sodium ions. Each system underwent energy minimization using the steepest descent method until the maximum force fell below 100 KJ/Mol nm^{-1}. Subsequently, the systems were equilibrated for 1 ns under the NVT ensemble, followed by an NPT ensemble for 5 ns. The NVT simulations utilized a V-rescale thermostat to maintain a temperature of 300 K (Bussi, Donadio, & Parrinello, 2007), while the NPT simulations employed the Berendsen barostat to maintain a pressure of 1 bar. Both equilibration simulations were conducted with a time step of 2 fs.

Afterward, the final frames of the restrained equilibration were used as starting points for 1 ns MD simulations with positional restraints on the ligand for structural relaxation. Following this, the simulations of the peptide and free ligand (without positional restraints) for 100 ns. Based on the structural trajectories, the root mean square deviations (RMSDs) of the backbone/ligand were calculated using Gromacs. The resulting structures were visually inspected using PyMol (v.4.6) and VMD 1.4.7, while the graphs were created using Xmgrace (Grace-5.1).

2.4. Calculation of binding energy

Utilizing the Poisson-Boltzmann surface area (MM/PBSA) method, the binding energy was calculated with the assistance of the gmx_MMPBSA tool as described by Valdes-Tresanco et al. (Valdes-Tresanco, Valdes-Tresanco, Valiente, & Moreno, 2021). For this purpose, we leveraged the trajectory data extracted from Gromacs and specifically employed the recorded data from the final 10 ns, considering the stability of the complex during the simulation. The evaluation of peptide binding affinity encompassed an analysis of various energetic components, including relative binding energy, vdW energy, polar solvation energy, electrostatic energy, and SASA energy.

2.5. Preparation of OTA − BSA conjugates

The conjugation of OTA to BSA was synthesized through the carbodiimide method with slight modifications (Becheva, Atanasova, Ivanov, & Godjevargova, 2020). NHS (1.2 mg) and EDC (1.6 mg) were dissolved in 200 μL of DMF, and then 1.0 mg OTA was added. The resulting mixture was left on a shaker at 25 °C for 1 h, following this, the mixture was incubated at 4 °C overnight. Then, 1 mg BSA dissolved in carbonate-bicarbonate buffer (0.1 M, pH 9.6) was added dropwise in the colorless mixture. The mixture solution appeared yellow, devoid of any sludge or insoluble components, then it was further left on a shaker at 25 °C for two hours. The final product was dialyzed in a 5 mmol L^{-1} phosphate buffered solution buffer (pH 7.4) at 4 °C for 72 h. The synthesized OTA-BSA conjugate solution, containing 50 % glycerol (*v*/v), was stored at −20 °C for future use.

2.6. Binding assessment by enzyme-linked peptide assay (ELPA)

The conjugate of OTA-BSA (20 μg mL^{-1}) dissolved in carbonate-bicarbonate buffer (50 mM, pH 9.6) was added to the microtiter plates and left to rest overnight at 4 °C. After washing with phosphate buffered solution containing 0.5 % Tween 20 (PBST), the plates were blocked using 0.5 % BSA solution for 2 h at room temperature. Next, biotin-labeled peptides ranging from 5 to 500 nM were added and incubated at 37 °C for 2 h. After incubation, a diluted (1:8000) high-sensitivity streptavidin-horse radish peroxidase (SA-HRP) conjugate was added to each well and left on a shaker at 37 °C for 30 min. Wells were then washed with PBST for 5 times, followed by the addition of TMB chromogen solution and further incubation at 37 °C for 30 min. The absorbance value was measured at a wavelength of 450 nm using a microplate reader after the introduction of 2 M sulfuric acid. The GraphPad Prism software was used to fit the binding saturation curves and determine the dissociation constant (K_d) values, using the eq. $Y = B_{max} \cdot X/(K_d + X)$. In this equation, Y represents the absorbance value at different concentrations of the peptide, B_{max} is the maximum absorbance value in the fitted curve, and X denotes the concentration of the peptide.

2.7. Preparation of NH_2-MIL-88(Fe)

NH_2-MIL-88(Fe) was synthesized following a previous research methodology, albeit with a few adjustments implemented (Qu et al., 2020). In detail, 0.544 g $FeCl_3$ and 0.812 g NH_2-BDC were dispersed in 12 mL and 18 mL dimethylformamide solution, respectively. After mixing the above two solutions, glacial acetic acid (3 mL) was added. Next, the mixture was placed into a Teffon-lined steel autoclave and heated at 120 degrees Celsius for a duration of 24 h. Following the reaction, the resulting solid was isolated through centrifugation and washed with a solution of DMF/ethanol. The material was gathered and further dried overnight under vacuum at 60 °C.

2.8. Design of the RHB-MRP-biosensor for OTA

The RHB labeled MRP was obtained by modifying RhB at the C-terminal. In order to maintain the functional integrity of the peptide containing 17 amino acids, RhB was modified on the added amino acid lysine. Thus, the sequence is KQRLKCASLQKFGERAFK-RhB, which is named Pep-RhB (Fig. 1A). The optically-active nanocrystal of NH_2-MIL-88(Fe) was selected as the absorbers and fluorophores in the detection system, and its fluorescence could be quenched due to the combination with RhB-MRP (Fig. 1B). When OTA was added, the competitive binding with the peptide would cause the dissociation of RhB-MRP from NH_2-MIL-88(Fe), resulting in a change in fluorescence (Fig. 1C).

2.9. Detection of OTA by RHB-MRP/NH_2-MIL-88(Fe) sensor

In a standard procedure, 5 mg of NH_2-MIL-88(Fe) was added to 50 mL of acetic acid - sodium acetate buffer (pH 5.5, 50 mmol L^{-1}), sonicated for 20 min to form a uniform solution. After reaction of the standard solution of OTA with Pep-RhB in the same buffer, the MOFs was added. The sample was then measured at an excitation wavelength of 360 nm.

2.10. Analysis of real samples

Fermentation food (homemade vinegar) and grains that used to make fermented foods are obtained from Yunnan and Jiangsu province. For solid samples, the sample of 5 g fine ground into powder was extracted with 20 mL methanol-deionized water (70:30 *v*/v) extraction solution and incubated in a shaker at room temperature for 30 min, then centrifuged at 10000 r/min for 10 min. The supernatant was passed through the 0.45um membrane to remove the particulate matter for further detection and for the spike recovery experiment. About the liquid samples, the sample of 5 mL was added into 15 mL methanol-deionized water (70:30 v/v) and incubated in a shaker for 30 min. The mixture was passed through 0.45 μm membrane for further detection and for the spike recovery experiment. Different concentrations of OTA were added during the extraction of several real samples to calculate the recovery of the method. The recovery was calculated using the formula: Recovery = (Measured concentration − Original sample concentration) / Known added concentration ×100.

2.11. Data analysis

Molecular dynamics simulation data were obtained using the *trjconv* tool in GROMACS (2022.3). Molecular structure images were processed using VMD (1.9.4) and PyMOL (2.5.2), while relevant statistical plots were analyzed and generated using Origin (2022). SPSS Statistics Software 27.0 was used for statistical analysis and the mean comparisons were analyzed by Duncan's multiple range test.

3. Results and discussion

3.1. The verification of peptide affinity based on MD simulations and ELPA

The peptide 195–211, termed 17-Pep was developed from the human serum albumin (HSA) using top-down computational design strategy. The design process refers to a method recently reported by our group (Yu et al., 2025) and is outlined in the **Supplementary Materials**. The MD simulations analyzed the interacting of the 17-Pep and OTA, it can be found that the 17-Pep unfolds into a flexible short chain and bind to the OTA in a semi-wrapped manner (Fig. 2A). In the 150 ns long simulations, RMSDs served as a key metric to quantify the conformational alterations in the simulated structures. Fig. 2B illustrates the temporal progression of RMSDs for 17-Pep (Backbone) and OTA to 17-Pep (Lig to backbone). In the latter half of the 17-Pep simulation, a stable plateau was achieved with fluctuations below 0.5 nm, signifying the attainment of equilibrium. Similarly, the RMSD of OTA binding to 17-Pep converged to a plateau with fluctuations less than 1 nm during the

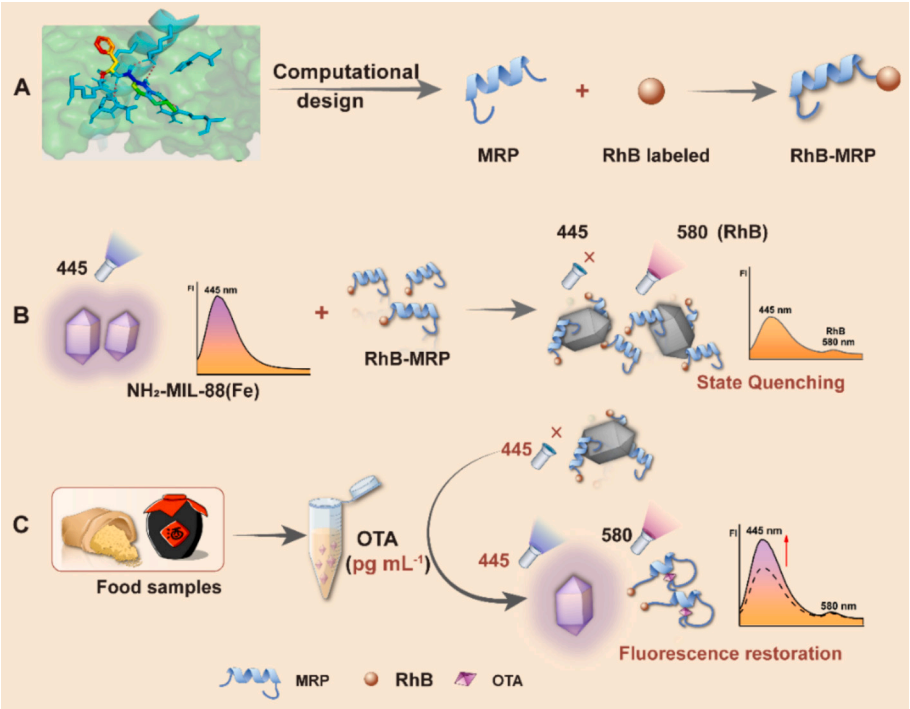

Fig. 1. Schematic diagram for the construction of fluorescence biosensor based on RHB-MRP and NH_2-MIL-88(Fe). (A) Design of MRP and Pep-RhB. (B) Synthesis of NH_2-MIL-88(Fe) and its fluorescence quenching upon interaction with RhB-MRP. (C) Fluorescence recovery of NH2-MIL-88(Fe) upon addition of OTA.

final 20 ns, demonstrating that the 17-Pep and OTA complex had achieved dynamic equilibrium.

Meanwhile, MD simulations spanning 100 nm for several structurally similar mycotoxins with 17-Pep in water environment were also performed to evaluate the relative specificity of 17-Pep, including aflatoxin B_1 (AFB_1), deoxynivalenol (DON), patulin (PAT), and zearalenone (ZEN). Obviously, the substantial fluctuations in the RMSDs of the ligand to backbone **(Fig. S4)**, exceeding 10 nm, indicate the difficulty in achieving a stable conformation and effective bonding between these mycotoxins and 17-Pep. The large RMSD fluctuations could also imply that the binding pocket is not fully complementary to the shape and flexibility of other mycotoxins, leading to less stable or transient binding states. This instability might contribute to poor binding affinity, further hindering the formation of a strong and reliable complex. Hydrogen bond analysis was performed to evaluate the binding between peptide and OTA. Hydrogen bonds formed between ligand and peptide are responsible for maintaining the oriented complex structure, where the flexibility of the peptide's residues contributes to the formation of bonds. The number of H bonds formed by the protein with the ligand molecules were calculated and depicted on Fig. 2C. The hydrogen bond number depicted that the 17-Pep formed H bonds from 0 (minimum) to 7 (maximum) during the 150 ns, maintaining 2–3H bonds in the most of the time for the complete simulation. The findings indicated that stable hydrogen bonds were capable of forming between peptides and polar groups present in OTA, a favorable characteristic that enhanced binding efficacy. Next, the binding energy of the complex was calculated utilizing MM/PBSA method shown in Fig. 2D. We found that the binding energy of OTA and 17-Pep is −77.6 KJ/Mol, which is significantly better than other structurally similar mycotoxins **(Fig. S5)**. The contribution of binding energy from each residue was also quantified, revealing that the initial and terminal residues of the peptide, specifically lysine, arginine, leucine, and phenylalanine, facilitate positive binding effects. Conversely, the intermediate residues (especially glutamic) exhibit a relatively negative binding propensity, aligning with the half-packet binding configuration observed in the Fig. 2A conformation.

The binding affinity of 17-Pep was assessed through an ELPA (Qi et al., 2023), and the corresponding schematic representation is depicted in Fig. 2E. The saturation binding curve, illustrated in Fig. 2F, exhibits a strong linearity with an R^2 value of 0.98. Binding affinity test to BSA as a control was shown in **Fig. S8**. The K_d, derived from quadratic curve fitting, was determined to be 12.18 ± 6.59 nM. Compared to reported MRPs for OTA, such as the affinity peptide towards OTA reported by Rahi, Lanjekar, and Ghormade (2022) with a Kd of 1.046 μM, 17-Pep exhibits significantly superior binding affinity for OTA. This result demonstrates its promising potential for OTA detection applications.

3.2. *Characterizations of NH_2-MIL-88(Fe)*

As depicted in the SEM images **(**Fig. 3A**)**, the NH_2-MIL-88(Fe) crystal exhibits a bi-conical prismatic morphology, characterized by an approximate 5 μm extension of their prismatic configuration, consistent with previous reports. The FT-IR spectroscopy was utilized to characterize the molecular structure of NH_2-MIL-88(Fe), as shown in Fig. 3B. The spectra clearly reveal vibrational bands of the -NH_2 groups located approximately at 3465 and 3373 cm^{-1} (Wan et al., 2022). Notably, protonated carboxylic groups, typically identified by a band near 1710 cm^{-1}, were absent in the spectra. This result further demonstrates that the two carboxylic groups in the 2-aminoterephthalic acid were deprotonated and coordinated with Fe^{3+} ions. Vibrations related to the Fe—O moieties showed as bands at 577, 516, and 428 cm^{-1}, further confirming the structural features of the NH_2-MIL-88(Fe) (Abbasian & Khayyatali-mohammadi, 2023). Furthermore, the XRD diffraction patterns **(**Fig. 3C**)** indicate a well-defined crystal structure, mirroring the diffraction peaks observed in the simulated NH_2-MIL-88(Fe), thus confirming its structural integrity (Wan et al., 2022). Additionally, the XPS spectrum displays peaks at 285.08, 399.08, 533.08, and 711.08 eV (Fig. 3D), corresponding to C 1 s, N 1 s, O 1 s, and Fe 2p, respectively, and confirming the successful synthesis of composite crystals.

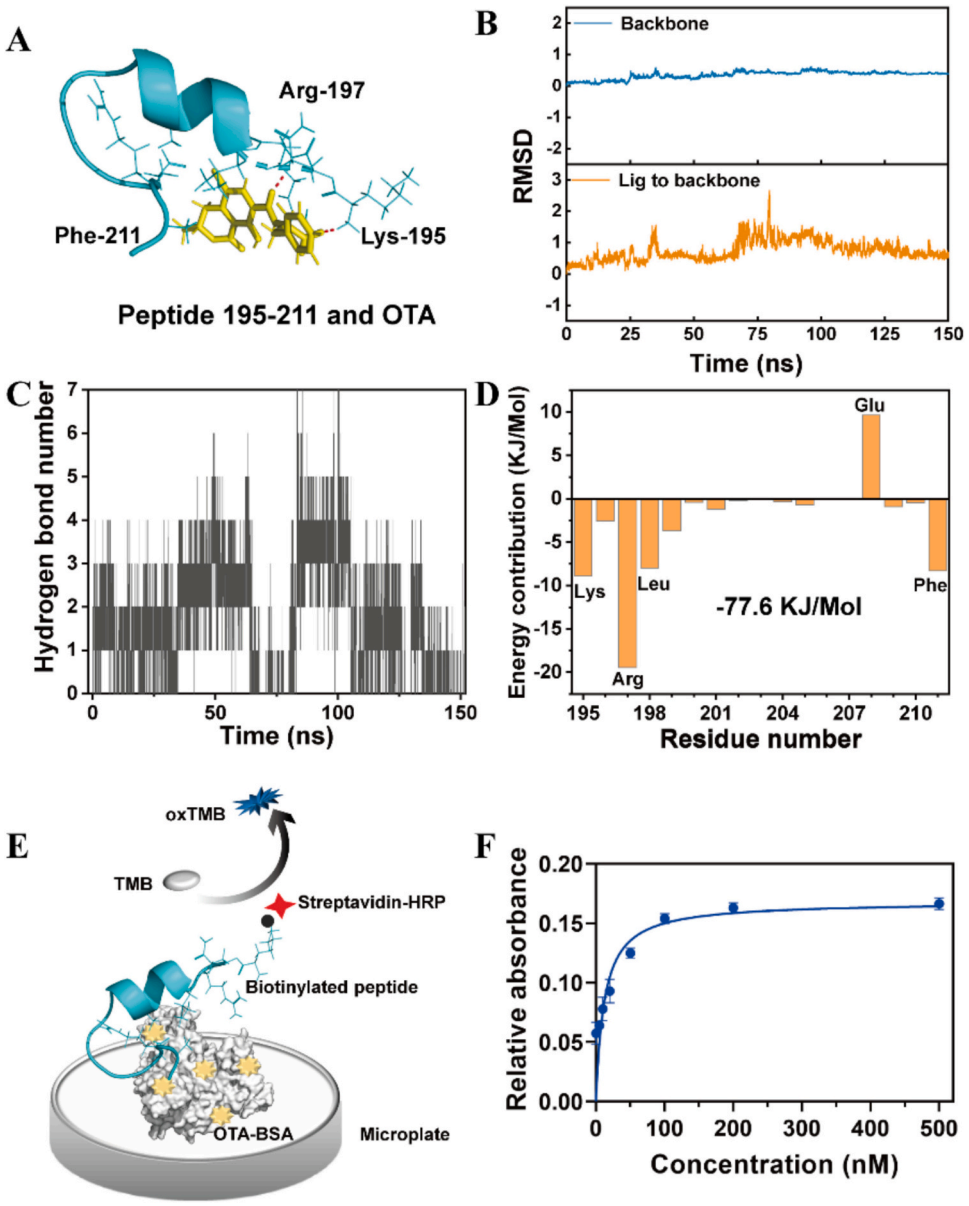

Fig. 2. (A) The conformation of 17-Pep (Peptide 195–211) and OTA at the last frame in the MD. (B) RMSD of the peptide backbone and lig to backbone (OTA to backbone) with respect to the initial configuration. (C) The hydrogen bond number profiles of OTA and 17-Pep during the MD. (D) The contribution of the residues in the 17-Pep to binding affinity and the binding affinity of the 17-Pep and OTA (−77.7KJ/Mol). (E) The corresponding schematic of the ELPA assay to assess the binding affinity between 17-Pep and OTA. (F) The saturation binding curve with concentration of OTA ranging from 0 to 500 nM.

3.3. Fluorescence response and the principle of the pep-RhB/NH_2-MIL-88 (Fe) sensor for OTA

The binding interactions between a short peptide and target, being difficult to obtain a direct measurable signal, pose a challenge for the design of a suitable transducer. To address this, we designed fluorophore labeled 17-Pep (Pep-RhB), and we found that the fluorescence of NH_2-MIL-88(Fe) (λ_{em} = 445 nm) could be quenched by Pep-RhB. Meanwhile, RhB serves as an inherent reference, enabling the correction of deviations stemming from environmental factors and variations in equipment. When OTA was added, the specific binding of Pep-RhB with OTA resulted in the fluorescence restoration in NH_2-MIL-88(Fe). The Pep-RhB effectively transforms the otherwise difficult to detect binding events into quantifiable optical signals. And the analysis of the Pep-RhB was shown in **Fig. S6–7**. Different from competitive reaction-based methods, such as the fluorescence resonance energy transfer approach reported by Su et al. (2022) for OTA detection, the Pep-RhB/NH_2-MIL-88(Fe) system does not require a labeled recognition element for the target, thereby reducing the risk of mycotoxin emissions.

As shown in Fig. 4 **A**, the fluorescence emission peak of NH_2-MIL-88 (Fe) at 445 nm (a) was quenched by Pep-RhB (b), at the same time the fluorescence emission peak of Pep-RhB was shown at 580 nm. While after incubation with high concentration of OTA (0.1 ng mL^{-1}) and the Pep-RhB conjugate, the fluorescence at 445 nm returns to its original level (c). Next, we investigated the change in fluorescence between NH_2-MIL-88(Fe) and RhB, it can be found that the fluorescence of NH_2-MIL-88(Fe) also can be quenched by RhB, while the adding of OTA (0.1 ng mL^{-1}) in the reaction system did not observe the restoration at 445 nm as above (Fig. 4**B**). Based on the fluorescence changes, 17-Pep can be confirmed to have a crucial effect for the fluorescence recovery due to the interaction with OTA. The fluorescence changes demonstrated that the affinity binding of OTA with MRP is the key to fluorescence restoration. We also investigated the effect of non-fluorescently labeled peptides on the fluorescence of NH_2-MIL-88(Fe), as shown in **Fig. S9**. It

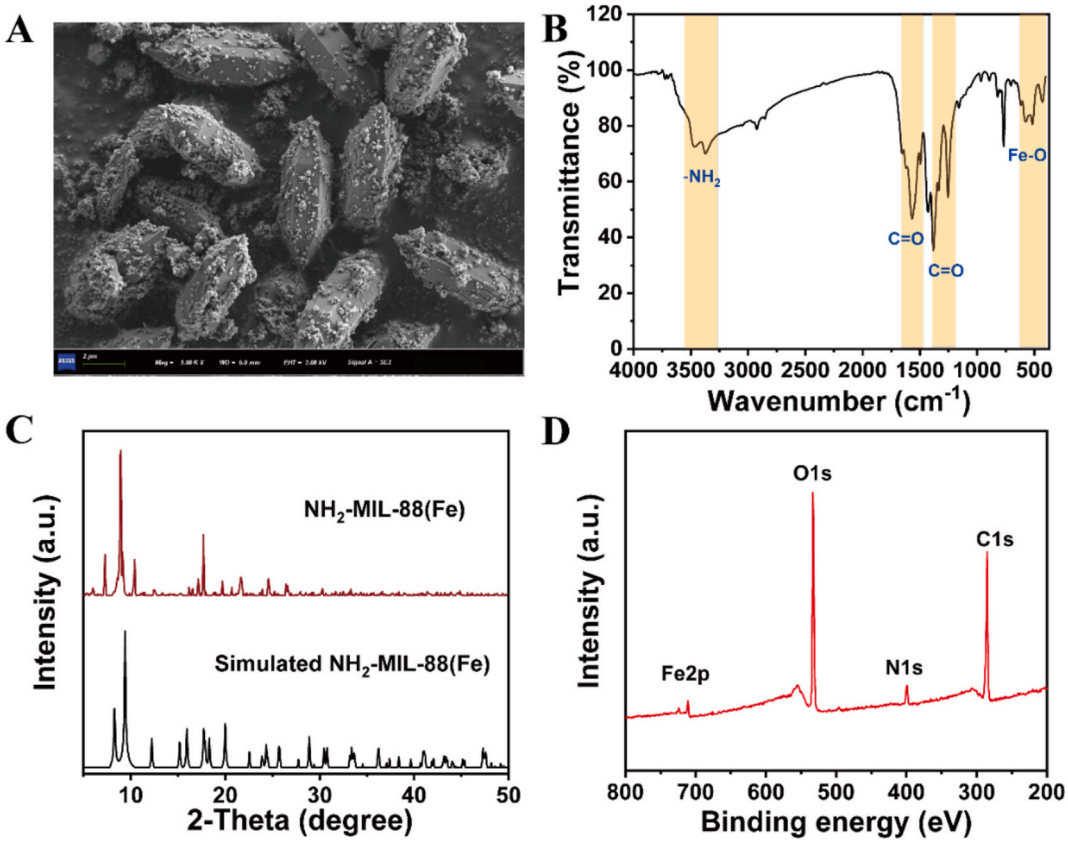

Fig. 3. The analysis of NH_2-MIL-88(Fe): (A) SEM image. (B) FT-IR analysis of the functional vibrations. (C) XRD Patterns Comparison: Theoretical vs. Experimentally Synthesized. (D) Surface elemental composition by XPS survey.

can be found that the fluorescence at I_{445} of NH_2-MIL-88(Fe) exhibited almost no change before and after the addition of the peptide, indicating that the peptide alone also does not affect the fluorescence of NH_2-MIL-88(Fe).

Next, the machine of RHB-MRP mediated fluorescence sensing strategy for OTA was explored and verified. Firstly, about the fluorescence of NH_2-MIL-88(Fe) quenched by Pep-RhB, the mechanism usually contains dynamic quenching, static quenching, and inner filter effect (Zhang et al., 2019; Zu et al., 2017). To elucidate the underlying quenching mechanism, the fluorescence lifetime of the fluorophore was examined, as it remains relatively constant in static quenching and inner filter effect (IFE) processes but undergoes changes in dynamic quenching. Consequently, fluorescence decay curves were recorded for both NH_2-MIL-88(Fe) with and without Pep-RhB, providing insights into the precise quenching mechanism at play. As illustrated in Fig. 4**C**, the data were well fitted with a biexponential equation. Upon the addition of Pep-RhB, the fluorophore's average fluorescence lifetime shifted from approximately 13.90 ns (τ0) to 14.03 ns (τ1). The value of τ_0/τ_1 is approximately 1, indicating fluorescence lifetime after adding Pep-RhB was almost constant with the absence of it. The results identified that the perturbation of the energy donor (fluorophore) occurs in ground state rather than occurring at the excited state. Thus, the possibility of dynamic quenching that occurred at the excited state accompanied by the fluorescence lifetime change is excluded.

To gain a precise understanding of the quenching mechanism in this system, UV–vis absorption spectra were recorded for the three reaction systems (Fig. 4**D**). As evident from Fig. 4**D**, the UV–vis absorption spectrum of NH_2-MIL-88(Fe)/Pep-RhB system and the sum absorption spectrum between NH_2-MIL-88(Fe) and Pep-RhB were not superposed within experimental error, suggesting the formation of a ground state complex between NH_2-MIL-88(Fe) and RHB-MRP. Furthermore, compared to the summed spectrum, the absorption spectrum of NH_2-MIL-88(Fe)/Pep-RhB system showed an obvious decrease at 578 nm, indicative of a hypochromic effect upon the formation of the NH_2-MIL-88(Fe)/Pep-RhB complex (S. Huang et al., 2015). In addition, the Zeta potential (Fig. 4**F**) of NH_2-MIL-88(Fe) (10 mg L^{-1}) is about −0.5 mV (a), after mixing with Pep-RhB (5 mg L^{-1}), the Zeta potential jumped to 21.8 mV (b), the jump in the absolute value of the Zeta potential indicates that a more stable complex has formed in the system. While upon the increasing concentration of added OTA, the Zeta potential of the mixture gradually decreased (c-f). These provide evidence that NH_2-MIL-88(Fe) and Pep-RhB form a more stable complex, and after adding OTA, OTA and MOFs competitively bind Pep-RhB, causing the dissociation of the Pep-RhB/MOFs complex. Static quenching is a non-radiative process in which the emission of a fluorophore is reduced due to the formation of a ground-state complex between the fluorophore and a quencher molecule. By analyzing the spectra and Zeta potential, it can be concluded that the fluorescence of NH_2-MIL-88(Fe) was quenched by Pep-RhB due to the formation of a ground-state complex, consistent with the mechanism of static quenching. Upon the addition of OTA, the quenching effect was disrupted, leading to fluorescence restoration.

From Fig. 4**E** and **Fig. S10**, it can be found that the absorption of Pep-RhB with the excitation and emission spectrum of NH_2-MIL-88(Fe) all overlapped, suggested that the quenching machine may be caused by IFE. Notably, this IFE phenomenon also primarily manifests as a decrease in fluorescence intensity, without altering the characteristic decay time of the emission. Thus, further analysis was conducted as shown in **Fig. S11**, it can be found that the fluorescence quenching was irregular upon introduction of increasing amounts of Pep-RhB, this phenomenon did not fit the Parker equation (**Eq. S1**) which can reflect the IFE process (S. Huang et al., 2015). Therefore, it can be determined that the quenching process is controlled by only static quenching.

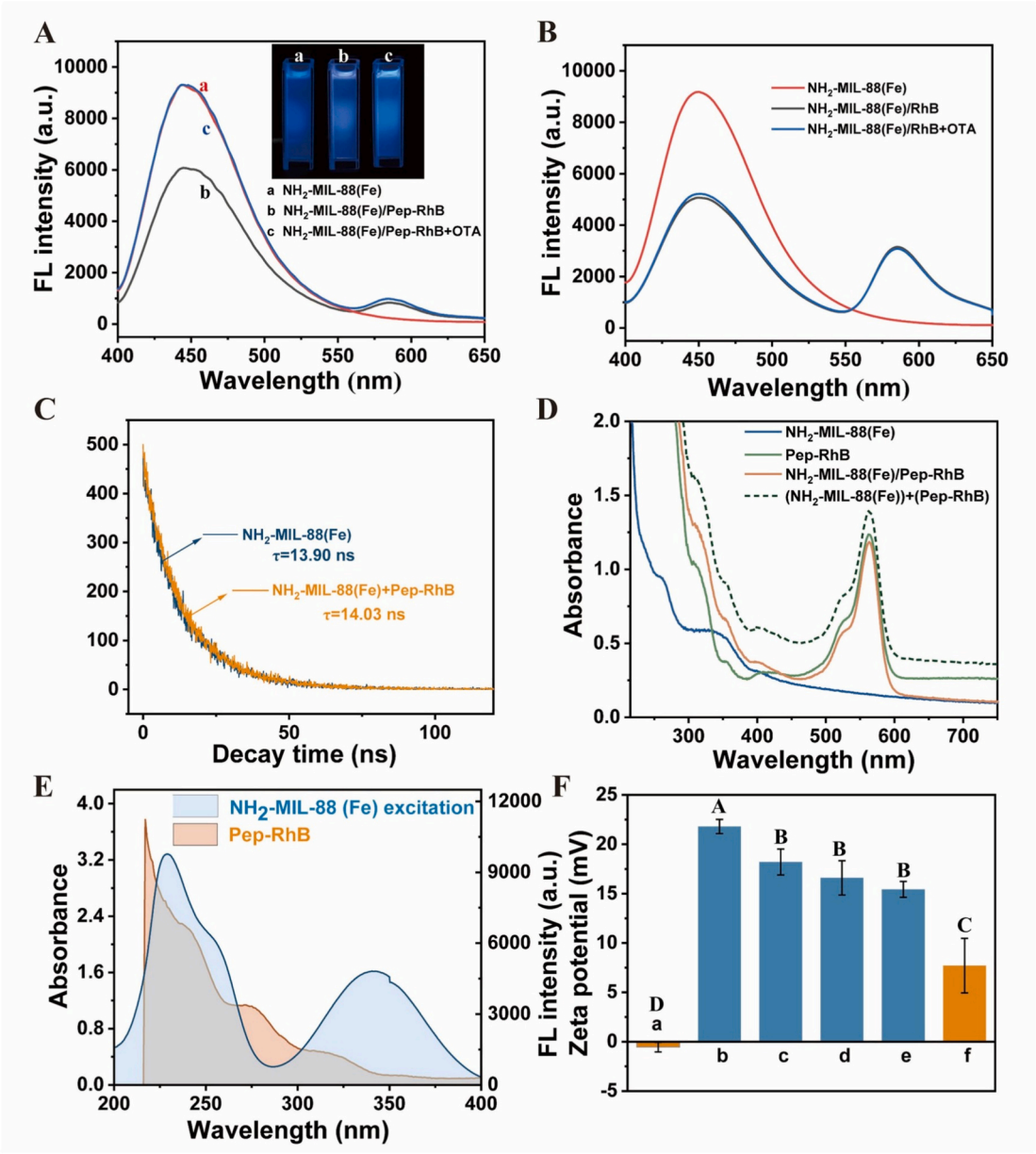

Fig. 4. (A) and (B) Fluorescence spectra of different system. (C) Time resolved fluorescence spectra of NH_2-MIL-88(Fe) before and after Pep-RhB adding. All measurements were made at $\lambda_{em} = 430$ nm. τ is the fluorescence decay time. (D) UV–vis absorption spectra of different system; the sum absorption spectrum between NH_2-MIL-88(Fe) and Pep-RhB, respectively. NH_2-MIL-88(Fe): 20 mg L^{-1}; Pep-RhB: 200 mg L^{-1}. (E) Spectral overlap between the excitation of NH_2-MIL-88(Fe) and the absorption of Pep-RhB. (F) The Zeta potential of NH_2-MIL-88(Fe) (10 mg L^{-1}) (a), NH_2-MIL-88(Fe) (10 mg L^{-1}) mixing with Pep-RhB (5 mg L^{-1}) (b), NH_2-MIL-88 (Fe) (10 mg L^{-1}) + Pep-RhB (5 mg L^{-1}) + 4 ng L^{-1} OTA (c), NH_2-MIL-88(Fe) (10 mg L^{-1}) + Pep-RhB (5 mg L^{-1}) + 8 ng L^{-1} OTA (d), NH_2-MIL-88(Fe) (10 mg L^{-1}) + Pep-RhB (5 mg L^{-1}) + 10 ng L^{-1} OTA (e), Pep-RhB (5 mg L^{-1}) + 4 ng L^{-1} OTA (f). Different capital letters indicated significant differences ($P < 0.05$).

3.4. Optimization of the detection conditions for the pep-RhB/NH_2-MIL-88(Fe) fluorescence sensor

To optimize the efficacy of the fluorescence sensor, a comprehensive investigation and assessment of multiple parameters that could potentially modulate its sensitivity were undertaken. These encompassed varying the concentrations of NH_2-MIL-88(Fe) and Pep-RhB, adjusting the pH level of the reaction buffer, exploring different incubation durations for the Pep-RhB with OTA, and analyzing the fluorescence quenching time.

The concentration of the probe plays a crucial role in determining the fluorescence intensity, which directly impacts the sensitivity and accuracy of the biosensor. To investigate the optimal probe concentration, the variation in the I_{445}/I_{580} ratio ($\Delta I_{445}/I_{580}$) was tested for MOFs concentrations ranging from 10 to 30 mg L^{-1} (Fig. 5A). As the concentration of the probe increased, both the I_{445}/I_{580} ratio before and after the addition of OTA exhibited a noticeable upward trend. The maximum $\Delta I_{445}/I_{580}$ was observed at a probe concentration of 20 mg L^{-1}, indicating that this concentration facilitates the most effective fluorescence quenching. The static quenching effect is more efficient at this concentration, possibly because it strikes an optimal balance between the number of available MOFs sites for Pep-RhB binding and the overall quenching efficiency (Sun et al., 2022). At concentrations below 20 mg L^{-1}, the quenching effect is less pronounced, likely due to fewer probe molecules interacting with Pep-RhB. Conversely, at concentrations above 20 mg L^{-1}, although more probe molecules are available, the quenching efficiency may plateau or even decrease due to factors such as increased aggregation of the MOFs or a reduced availability of effective

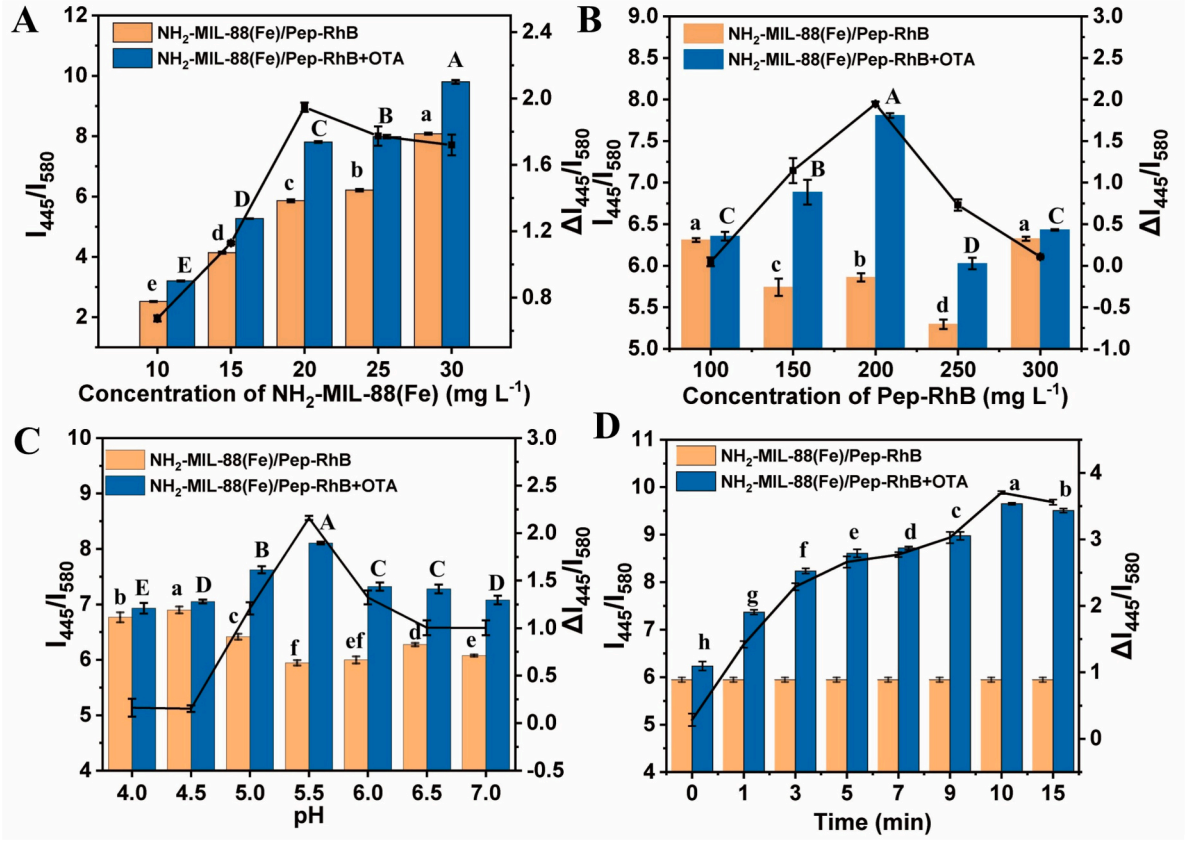

Fig. 5. The radio of I_{445} and I_{580} before and after OTA adding with different (A) concentration of NH_2-MIL-88(Fe), (B) concentration of Pep-RhB, (C) pH, and (D) incubation time of MRP and OTA. The accompanying error bars indicate the standard deviation derived from three replicate measurements. Different capital/lowercase letters indicated significant differences ($P < 0.05$).

binding sites. Additionally, NH_2-MIL-88(Fe) may release metal ions (Fe^{2+} or Fe^{3+}) under certain environmental conditions, which, at high concentrations, could be toxic to aquatic organisms, plants, and microorganisms. Using a lower concentration of NH_2-MIL-88(Fe) helps minimize potential environmental impact while ensuring the method remains both effective and environmentally friendly.

The concentration of Pep-RhB also important for the detection system, as it serves both in the recognition process and in mediating fluorescence quenching. As shown in Fig. 5B, we investigated Pep-RhB concentrations of 100, 150, 200, 250, and 300 mg L^{-1}. It can be found that the quenching effect did not show a straightforward positive correlation with the concentration of Pep-RhB. At lower concentrations, fluorescence quenching may be less efficient due to limited interactions between Pep-RhB and NH_2-MIL-88(Fe), resulting in a less noticeable fluorescence recovery after interaction with the analyte (OTA). However, as the concentration of Pep-RhB increases, a saturation effect could occur, where excessive probe molecules might lead to aggregation or inefficient energy transfer, thus reducing the quenching efficiency (Dawson et al., 2023). The complex balance between probe concentration, binding site availability, and quenching efficiency may explain the observed lack of a direct positive correlation. Thus, 20 mg L^{-1} was identified as the optimal concentration for detecting OTA.

The fluorescence intensity of NH_2-MIL-88(Fe) and the interaction of Pep-RhB and OTA were all influenced by pH, making it also important for the sensitivity of the fluorescence sensor. The pH ranging from 4.0 to 7.0 was investigated and is shown in Fig. 5C. When the pH is at 4.0 and 4.5, the $\Delta I_{445}/I_{580}$ remains unchanged, indicating that at these acidic conditions, the interaction between Pep-RhB and NH_2-MIL-88(Fe) may be weak or hindered, possibly due to protonation of functional groups on the NH_2-MIL-88(Fe) surface, which reduces binding affinity and fluorescence quenching efficiency. At 5.0 and 5.5, the $\Delta I_{445}/I_{580}$ keeps increasing, suggesting that at these slightly acidic conditions, the interaction between Pep-RhB and OTA is more favorable. At 6.0, 6.5 and 7.0, the $\Delta I_{445}/I_{580}$ decreases and remains stable. This could be due to the deprotonation of functional groups on both Pep-RhB and the NH_2-MIL-88(Fe) at higher pH, reducing the strength of interactions and thus lowering the quenching effect. Thus, at a pH of 5.5, not only is the quenching effect relatively strong and the I_{445}/I_{580} lower, but the restoration of fluorescence is also better, resulting in the difference of I_{445}/I_{580} ($\Delta I_{445}/I_{580}$) being maximum.

Fig. 5D depicts the variations in I_{445}/I_{580} and $\Delta I_{445}/I_{580}$ as a function of the incubation period between Pep-RhB and OTA. As the interaction time between the Pep-RhB and OTA intensified, a noticeable enhancement in the recovery of fluorescence intensity was observed. At an incubation time of 10 min, the fluorescence intensity peaked and remained stable within the experimental margin of error. Furthermore, an assessment of quenching time, presented in **Fig. S12**, revealed no significant variations in $\Delta I_{445}/I_{580}$ enhancement. Consequently, to ensure consistency, a reaction time of 1 min was selected for subsequent experiments. Moreover, the photostability of Pep-RhB and NH_2-MIL-88 (Fe) was also investigated and was shown in **Fig.S13**.

3.5. Evaluation of the detection capability of the pep-RhB/NH_2-MIL-88 (Fe) fluorescence sensor

Under the optimized conditions, the devised Pep-RhB/NH_2-MIL-88 (Fe) fluorescence sensor was employed to detect OTA concentration range from 5 to 100 pg mL^{-1}. As OTA concentrations increased, there was a corresponding increase in fluorescence intensity, which correlated with OTA concentration (C_{OTA}, pg mL^{-1}) within the 5 to 100 pg mL^{-1}

range. This relationship followed a calibration function described by $\Delta I_{445}/I_{580} = 2.15\lg C_{OTA}$-1.14, with a determination coefficient (R^2) of 0.9992 (**Fig. 6AB**). The limit of detection (LOD) was estimated to be 0.32 pg mL^{-1} (S/N = 3). In **Table S2**, we present a comprehensive comparison of our developed biosensor with various OTA detection methods reported in the literature. Even compared to OTA detection methods based on aptamers and antibodies, the Pep-RhB/NH_2-MIL-88 (Fe) fluorescence sensor exhibits a more sensitive LOD. The biosensor, leveraging a high-affinity MRP, offers a distinct advantage in sensitivity (**Table S2**). Additionally, its operational simplicity and rapid detection time (11 min) highlight its promising potential for quick and efficient analysis of OTA in food safety.

To validate the selectivity of the RHB-MRP-mediated biosensor for OTA detection, four other commonly co-occurring mycotoxins in grains (AFB_1, DON, PAT, ZEN, and FB_1) were tested. The concentrations of the target OTA and its analogs were set at 70 and 350 pg mL^{-1}, respectively, and the results are depicted in Fig. 6C. Notably, a significant alteration in $\Delta I_{445}/I_{580}$ was exclusively observed upon OTA addition, in contrast to the structurally similar toxins. This underscores the high selectivity of the 17-Pep towards OTA. Further analysis of the sensor's anti-interference capability (Fig. 6D) revealed that even in the presence of these structurally similar mycotoxins, the sensor maintained consistent fluorescence intensity, underscoring the robust anti-interference properties of MRP-based fluorescence sensing strategy.

3.6. Detection of OTA toxin in grain and fermentation food samples

The developed biosensing method was validated by analyzing a quality control sample (MRM-OC) of wheat flour for OTA. The determined concentration of OTA in MRM-OC, utilizing the fluorescence sensing strategy, was 13.20 ± 0.46 ng kg^{-1} (n = 3), which closely aligns with the certified value of 12.21 ng kg^{-1}, thereby attesting to the accuracy of the developed method. Therefore, a straightforward standard calibration method was employed for the quantification of OTA in authentic samples. As illustrated in Table 1, our analysis revealed the presence of OTA in Rice wine koji and wheat samples at concentrations of 8.74 and 7.80 ng kg^{-1}, respectively, both of which fell below the permissible limits set by the European Union. To validate the accuracy of our developed method, we spiked food samples with varying concentrations of OTA (10 and 20 ng kg^{-1}). The recovery rates achieved varied

Table 1
Analytical results for the determination of OTA in food samples.

Samples	Fluorescence sensor				HPLC-MS
	Added (ng kg^{-1})	Found (ng kg^{-1})	Recovery (%)	RSD[a] (%)	Found (ng kg^{-1})
Rice wine koji	0	8.74	–	6.7	8.70
	10	19.95	114.1	4.6	18.68
	20	30.02	109.3	5.4	20.11
Rose vinegar	0	ND[b]	–	–	ND
	10	10.58	105.8	5.7	10.03
	20	21.42	107.1	6.8	20.07
Oat	0	ND[b]	–	–	ND
	10	9.30	87.4	5.9	9.62
	20	18.75	93.8	5.2	19.58
Maize	0	ND[b]	–	–	ND
	10	10.63	106.3	8.3	10.13
	20	20.86	104.3	7.4	20.06
Wheat	0	7.80	–	6.6	8.29
	10	18.67	108.7	5.8	18.77
	20	26.39	106.2	5.3	28.46

RSD: Relative Standard Deviation, calculated as (Standard Deviation / Mean) × 100%.
ND: Not found.

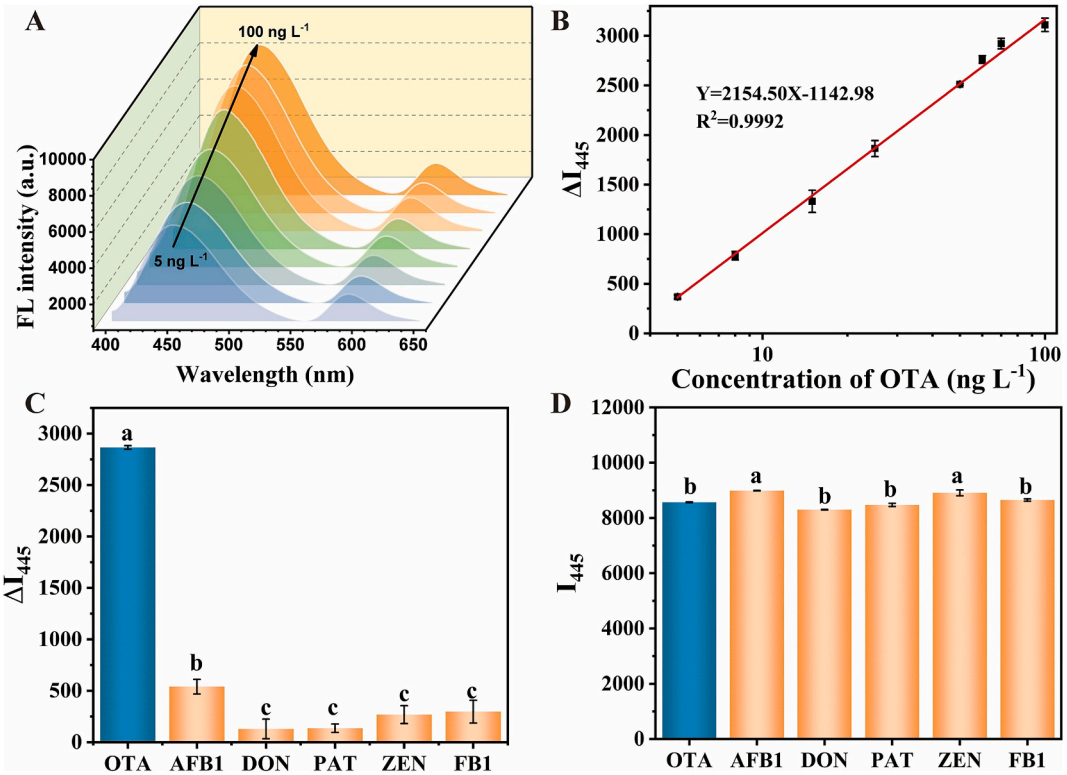

Fig. 6. (A) The spectra upon gradual addition of OTA (5–100 pg mL^{-1}). (B) The linear range of the sensor for OTA detection. (C) Selectivity of the biosensor for OTA (70 pg mL^{-1}) and other possible interfering toxins in food including AFB_1, DON, PAT, ZEN, and FB_1 (350 pg mL^{-1}). (D) Fluorescence intensity at 445 nm by OTA (70 pg mL^{-1}) in the absence and presence of other possible interfering toxins including AFB_1, DON, PAT, ZEN, and FB_1 (350 pg mL^{-1}). The accompanying error bars indicate the standard deviation derived from three replicate measurements. Different lowercase letters indicated significant differences ($P < 0.05$).

between 87.4 % and 114.1 %, and the relative standard deviation (RSD) does not exceed 6.7 %, demonstrating the high accuracy and dependability of our method for OTA detection in real samples.

4. Conclusion

In conclusion, we developed a sensitive and straightforward fluorescence approach utilizing high-affinity MRP for OTA detection. The MRP was designed from non-specific binding protein utilizing molecular simulation and a novel fluorometric probe RhB-MRP was synthesized. The probe allows for an indirect yet accurate representation of the MRP's binding to the target, and the introducing of fluorescent nanomaterials enables the binding changes to be sensitively captured. Moreover, we have explored the mechanism of fluorescence alterations in details, resulting in the development of a user-friendly fluorescence biosensor, which holds the potential for real-world applications for OTA detection in food samples, including cereals and fermented foods. The unexpected high affinity peptide with fluorophore modified paves a way to simplified and sensitive detection and further broadens the application of peptides in recognition technology.

CRediT authorship contribution statement

Li-Hong Yu: Writing – original draft, Methodology, Investigation, Conceptualization. **Yue-Hong Pang:** Writing – review & editing, Data curation, Conceptualization. **Xiao-Fang Shen:** Writing – review & editing, Project administration, Funding acquisition.

Declaration of competing interest

The authors declare that they have no known competing financial interests or personal relationships that could have appeared to influence the work reported in this paper.

Acknowledgment

We greatly appreciate the financial support from the National Natural Science Foundation of China (22476068, 22076067).

Appendix A. Supplementary data

Supplementary data to this article can be found online at https://doi.org/10.1016/j.foodchem.2025.143482.

Data availability

Data will be made available on request.

References

Abbasian, M., & Khayyatalimohammadi, M. (2023). Ultrasound-assisted synthesis of MIL-88(Fe) conjugated starch-Fe(3)O(4) nanocomposite: A safe antibacterial carrier for controlled release of tetracycline. *International Journal of Biological Macromolecules, 234*, Article 123665. https://doi.org/10.1016/j.ijbiomac.2023.123665

Ahn, S., Lee, S., Lee, J., & Kim, B. (2016). Accurate determination of ochratoxin a in Korean fermented soybean paste by isotope dilution-liquid chromatography tandem mass spectrometry. *Food Chemistry, 190*, 368–373. https://doi.org/10.1016/j.foodchem.2015.05.114

Becheva, Z. R., Atanasova, M. K., Ivanov, Y. L., & Godjevargova, T. I. (2020). Magnetic nanoparticle-based fluorescence immunoassay for determination of Ochratoxin a in Milk. *Food Analytical Methods, 13*, 2238–2248. https://doi.org/10.1007/s12161-020-01848-7

Bussi, G., Donadio, D., & Parrinello, M. (2007). Canonical sampling through velocity rescaling. *The Journal of Chemical Physics, 126*(1), Article 014101. https://doi.org/10.1063/1.2408420

Chen, J. Y., Wei, Q. X., Yang, L. Y., Li, J. Y., Lu, T. C., Liu, Z. J., & Xu, X. W. (2022). Multimodal Ochratoxin A-Aptasensor using 3'-FAM-enhanced exonuclease I tool and magnetic microbead carrier. *Analytical Chemistry, 94*(31), 10921–10929. https://doi.org/10.1021/acs.analchem.1c05576

Cruz-Aguado, J. A., & Penner, G. (2008). Determination of Ochratoxin a with a DNA aptamer. *Journal of Agricultural and Food Chemistry, 56*(22), 10456–10461. https://doi.org/10.1021/jf801957h

Dawson, W. M., Shelley, K. L., Fletcher, J. M., Scott, D. A., Lombardi, L., Rhys, G. G., & Woolfson, D. N. (2023). Differential sensing with arrays of de novo designed peptide assemblies. *Nature Communications, 14*(1), 383. https://doi.org/10.1038/s41467-023-36024-y

Gao, S., Zheng, X., Tang, Y., Cheng, Y., Hu, X., & Wu, J. (2019). Development of a fluorescently labeled aptamer structure-switching assay for sensitive and rapid detection of Gliotoxin. *Analytical Chemistry, 91*(2), 1610–1618. https://doi.org/10.1021/acs.analchem.8b05094

Guo, H., Ma, P., Li, K., Zhang, S., Zhang, Y., Guo, H., & Wang, Z. (2022). A novel ratiometric aptasensor based on dual-emission fluorescent signals and the conformation of G-quadruplex for OTA detection. *Sensors and Actuators B: Chemical, 358*. https://doi.org/10.1016/j.snb.2022.131484

Guo, P., Wang, Y., & Zhuang, Q. (2019). Highly sensitive and selective biosensor for heparin detection with rhodamine B-labelled peptides as fluorescent bioreceptors. *Sensors and Actuators B: Chemical, 299*. https://doi.org/10.1016/j.snb.2019.126873

Guo, Z., Tian, J., Cui, C., Wang, Y., Yang, H., Yuan, M., & Yu, H. (2021). A label-free aptasensor for turn-on fluorescent detection of ochratoxin a based on SYBR gold and single walled carbon nanohorns. *Food Control, 123*. https://doi.org/10.1016/j.foodcont.2020.107741

Homma, C., Tsukiiwa, M., Noguchi, H., Tanaka, M., Okochi, M., Tomizawa, H., & Hayamizu, Y. (2023). Designable peptides on graphene field-effect transistors for selective detection of odor molecules. *Biosensors and Bioelectronics, 224*, Article 115047. https://doi.org/10.1016/j.bios.2022.115047

Huang, J., Xu, Y., Xue, Y., Huang, Y., Li, X., Chen, X., & Ji, J. (2023). Identification of potent antimicrobial peptides via a machine-learning pipeline that mines the entire space of peptide sequences. *Nature Biomedical Engineering, 7*(6), 797–810. https://doi.org/10.1038/s41551-022-00991-2

Huang, S., Wang, L., Huang, C., Xie, J., Su, W., Sheng, J., & Xiao, Q. (2015). A carbon dots based fluorescent probe for selective and sensitive detection of hemoglobin. *Sensors and Actuators B: Chemical, 221*, 1215–1222. https://doi.org/10.1016/j.snb.2015.07.099

Mascini, M., Dikici, E., Perez-Erviti, J. A., Deo, S. K., Compagnone, D., & Daunert, S. (2021). A new class of sensing elements for sensors: Clamp peptides for Zika virus. *Biosensors and Bioelectronics, 191*. https://doi.org/10.1016/j.bios.2021.113471

Metzger, E. D., Brozek, C. K., Comito, R. J., & Dinca, M. (2016). Selective dimerization of ethylene to 1-Butene with a porous catalyst. *ACS Central Science, 2*(3), 148–153. https://doi.org/10.1021/acscentsci.6b00012

Neupane, L. N., Oh, E. T., Park, H. J., & Lee, K. H. (2016). Selective and sensitive detection of heavy metal ions in 100% aqueous solution and cells with a fluorescence Chemosensor based on peptide using aggregation-induced emission. *Analytical Chemistry, 88*(6), 3333–3340. https://doi.org/10.1021/acs.analchem.5b04892

Palazzesi, F., Prakash, M. K., Bonomi, M., & Barducci, A. (2015). Accuracy of current all-atom force-fields in modeling protein disordered states. *Journal of Chemical Theory and Computation, 11*(1), 2–7. https://doi.org/10.1021/ct500718s

Pandey, A. K., Samota, M. K., Kumar, A., Silva, A. S., & Dubey, N. K. (2023). Fungal mycotoxins in food commodities: Present status and future concerns. *Frontiers in Sustainable Food Systems, 7*. https://doi.org/10.3389/fsufs.2023.1162595

Qi, S., Dong, X., Niazi, S., Lu, M., Duan, N., & Wang, Z. (2023). Structure-guided engineering of aptamers to enhanced structural stability and application performance in alleviating β-lactoglobulin allergenicity. *Chemical Engineering Journal, 473*. https://doi.org/10.1016/j.cej.2023.145450

Qu, F., Wang, H., & You, J. (2020). Dual lanthanide-probe based on coordination polymer networks for ratiometric detection of glyphosate in food samples. *Food Chemistry, 323*, Article 126815. https://doi.org/10.1016/j.foodchem.2020.126815

Rahi, S., Lanjekar, V., & Ghormade, V. (2022). Development of a rapid dot-blot assay for Ochratoxin a (OTA) detection using peptide conjugated gold nanoparticles for bio-recognition and detection. *Food Control, 136*, 108842.

Ren, W., Pang, J., Ma, R., Liang, X., Wei, M., Suo, Z., & Liu, Y. (2022). A signal on-off fluorescence sensor based on the self-assembly DNA tetrahedron for simultaneous detection of ochratoxin a and aflatoxin B1. *Analytica Chimica Acta, 1198*, Article 339566. https://doi.org/10.1016/j.aca.2022.339566

Song, C.-G., Liu, Y.-Q., Ding, G., Yang, J., Wang, C.-Y., Wu, J.-R., & Yang, Y.-W. (2022). Synergistic Adsorption–Photocatalysis based on Magnetic Metal–Organic Framework Nanoplatforms for Organic Pollutant Removal. *ACS Applied Nano Materials, 5*(12), 18930–18939. https://doi.org/10.1021/acsanm.2c04734

Song, X., Ding, Q., Pu, Y., Zhang, J., Sun, R., Yin, L., & Liu, S. (2021). Application of the dimeric G-Quadruplex and toehold-mediated strand displacement reaction for fluorescence biosensing of ochratoxin a. *Biosensors and Bioelectronics, 192*, Article 113537. https://doi.org/10.1016/j.bios.2021.113537

Su, B., Zhang, Z., Sun, Z., Tang, Z., Xie, X., Chen, Q., & Hammock, B. D. (2022). Fluonanobody-based nanosensor via fluorescence resonance energy transfer for ultrasensitive detection of ochratoxin a. *Journal of Hazardous Materials, 422*, Article 126838. https://doi.org/10.1016/j.jhazmat.2021.126838

Sun, Z., Li, J., Tong, Y., Han, H., Yang, Y., Wang, C., & Jiang, Y. (2022). A ratiometric fluorescent biosensor based on self-fluorescent MOF and target-triggered rolling circle amplification for sensitive detection of exosome-derived miRNA. *Analytica Chimica Acta, 1221*, Article 340136. https://doi.org/10.1016/j.aca.2022.340136

Tao, F., Yao, H., Hruska, Z., Burger, L. W., Rajasekaran, K., & Bhatnagar, D. (2018). Recent development of optical methods in rapid and non-destructive detection of aflatoxin and fungal contamination in agricultural products. *TrAC Trends in Analytical Chemistry, 100*, 65–81. https://doi.org/10.1016/j.trac.2017.12.017

Valdes-Tresanco, M. S., Valdes-Tresanco, M. E., Valiente, P. A., & Moreno, E. (2021). gmx_MMPBSA: A new tool to perform end-state free energy calculations with

GROMACS. *Journal of Chemical Theory and Computation, 17*(10), 6281–6291. https://doi.org/10.1021/acs.jctc.1c00645

Wan, C. Q., Pang, Y. H., Feng, Y. W., & Shen, X. F. (2022). A ratio fluorescence sensor based on rhodamine B embedded metal-organic framework for glyphosate detection in Agri-food products. *Food Chemistry, 394*, Article 133446. https://doi.org/10.1016/j.foodchem.2022.133446

Wang, H., Zhao, B., Ye, Y., Qi, X., Zhang, Y., Xia, X., & Zhou, N. (2022). A fluorescence and surface-enhanced Raman scattering dual-mode aptasensor for rapid and sensitive detection of ochratoxin a. *Biosensors and Bioelectronics, 207*, Article 114164. https://doi.org/10.1016/j.bios.2022.114164

Wang, J., Zhang, J., Wang, J., Fang, G., Liu, J., & Wang, S. (2020). Fluorescent peptide probes for organophosphorus pesticides detection. *Journal of Hazardous Materials, 389*, Article 122074. https://doi.org/10.1016/j.jhazmat.2020.122074

Wang, S., Zong, Z., Xu, J., Yao, B., Xu, Z., Yao, L., & Chen, W. (2023). Recognition-activated primer-mediated exponential rolling circle amplification for signal probe production and ultrasensitive visual detection of Ochratoxin a with nucleic acid lateral flow strips. *Analytical Chemistry, 95*(44), 16398–16406. https://doi.org/10.1021/acs.analchem.3c03995

Wu, S., Xu, J., Chen, W., Wang, F., Tan, X., Zou, X., & Yan, S. (2024). Protein nanoscaffold enables programmable nanobody-luciferase immunoassembly for sensitive and simultaneous detection of aflatoxin B1 and ochratoxin a. *Journal of Hazardous Materials, 462*, Article 132701. https://doi.org/10.1016/j.jhazmat.2023.132701

Xu, G., Zhao, J., Yu, H., Wang, C., Huang, Y., Zhao, Q., & Liu, M. (2022). Structural insights into the mechanism of high-affinity binding of Ochratoxin a by a DNA aptamer. *Journal of the American Chemical Society, 144*(17), 7731–7740. https://doi.org/10.1021/jacs.2c00478

Xu, L., Wei, L., Shi, Q., Cai, C., Fu, H.-Y., & She, Y.-B. (2019). Non-targeted detection of multiple frauds in Orange juice using double water-soluble fluorescence quantum dots and Chemometrics. *Food Analytical Methods, 12*(11), 2614–2622. https://doi.org/10.1007/s12161-019-01570-z

Xu, W., Aikeremu, D., Wang, H., Li, J., & Li, H. (2023). Metal ion-peptide-intermediated ligand transfer for serum detection of the omicron variant of SARS-Cov-2 in echinococcosis patients. *Analytical Chemistry, 95*(25), 9513–9519. https://doi.org/10.1021/acs.analchem.3c00656

Yu, L., Yang, L., Cheng, S., Jiang, Q., Pang, Y., & Shen, X. (2025). Top-down computational Design of Molecule Recognition Peptides (MRPs) for enzyme-peptide self-assembly and chemiluminescent biosensing. *Analytical Chemistry, 97*(1), 355–364. https://doi.org/10.1021/acs.analchem.4c04295

Zhang, J., Zhou, R., Tang, D., Hou, X., & Wu, P. (2019). Optically-active nanocrystals for inner filter effect-based fluorescence sensing: Achieving better spectral overlap. *TrAC Trends in Analytical Chemistry, 110*, 183–190. https://doi.org/10.1016/j.trac.2018.11.002

Zhu, Q., & Zhou, X. (2022). A colorimetric sandwich-type bioassay for SARS-CoV-2 using a hACE2-based affinity peptide pair. *Journal of Hazardous Materials, 425*. https://doi.org/10.1016/j.jhazmat.2021.127923

Zu, F., Yan, F., Bai, Z., Xu, J., Wang, Y., Huang, Y., & Zhou, X. (2017). The quenching of the fluorescence of carbon dots: A review on mechanisms and applications. *Microchimica Acta, 184*(7), 1899–1914. https://doi.org/10.1007/s00604-017-2318-9